**Supplementary information**

**Loss-free Pulverization by Confining Copper Oxide inside Hierarchical Nitrogen-doped Carbon Nanocages toward Superb Potassium-ion Batteries**

Guanghai Chen,[a] Jia Liu,[a] Shenglan Ma,[a] Changkai Zhou,[a] Jietao Jiang,[a] Zhen Shen,[a] Lijie Yan,[a] Yue Guo,[a] Lijun Yang,[a] Qiang Wu,*[a] Xizhang Wang,*[a] Zheng Hu,*[a]

[a] Key Laboratory of Mesoscopic Chemistry of MOE and Jiangsu Provincial Lab for Nanotechnology, School of Chemistry and Chemical Engineering, Nanjing University, Nanjing 210023, China.

∗ **Corresponding authors.**

E-mail: wqchem@nju.edu.cn; wangxzh@nju.edu.cn; zhenghu@nju.edu.cn
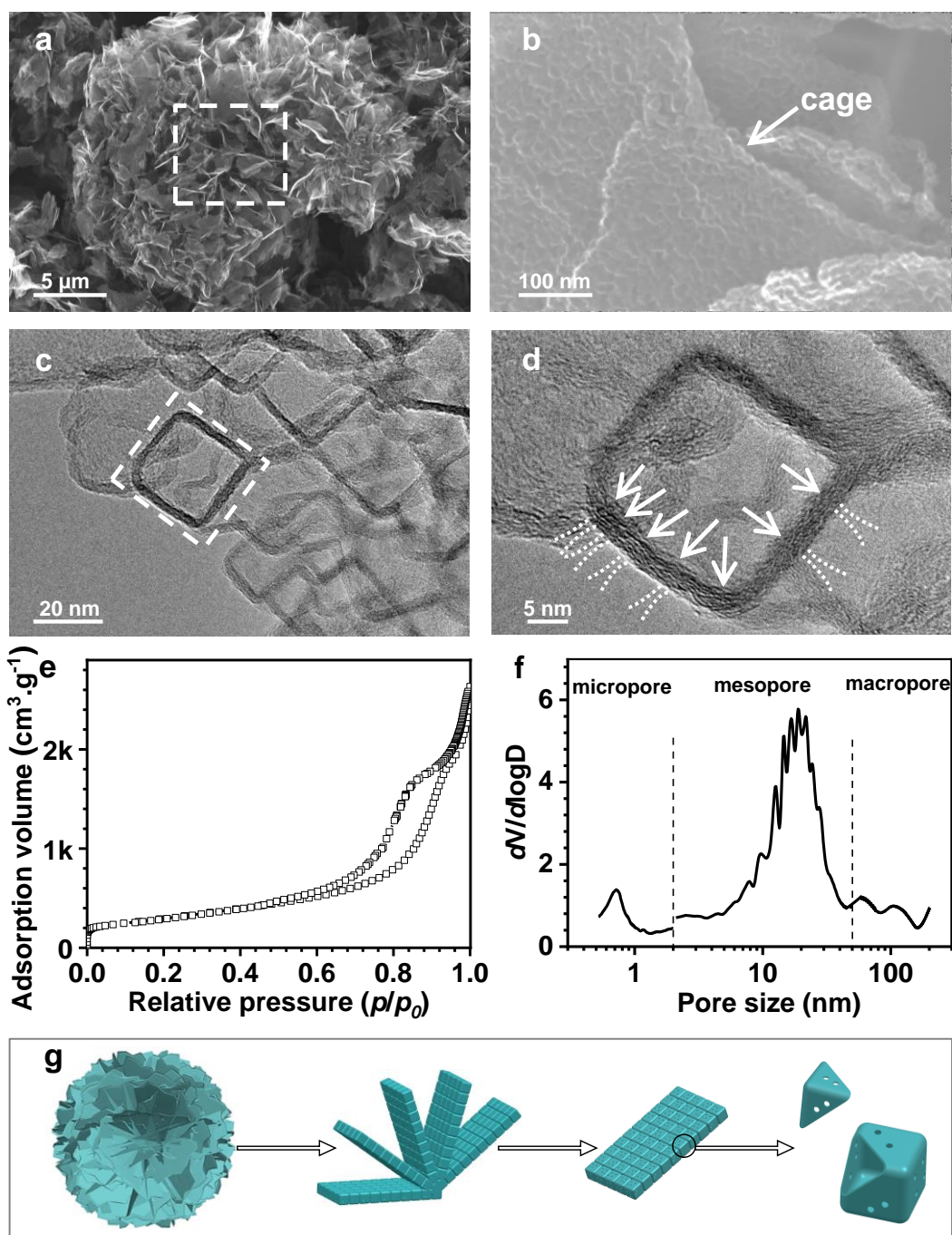
**Fig. S1 Morphology and structural characterizations of hNCNC.** (a,b) SEM images. (c,d) HRTEM images. (e,f) N₂ adsorption-desorption isotherm and corresponding pore size distribution. (g) Schematic structural characters of the hNCNC.

Abundant micropores across the nanocage wall are observed, with a size of ca. 0.6 nm (Fig. S1d,f). Detailed parameters of hNCNC are listed in Table S1.

The size of the micropores is much smaller than the size of the encapsulated Cu-based active components, which ensures the loss-free pulverization during charge/discharge.
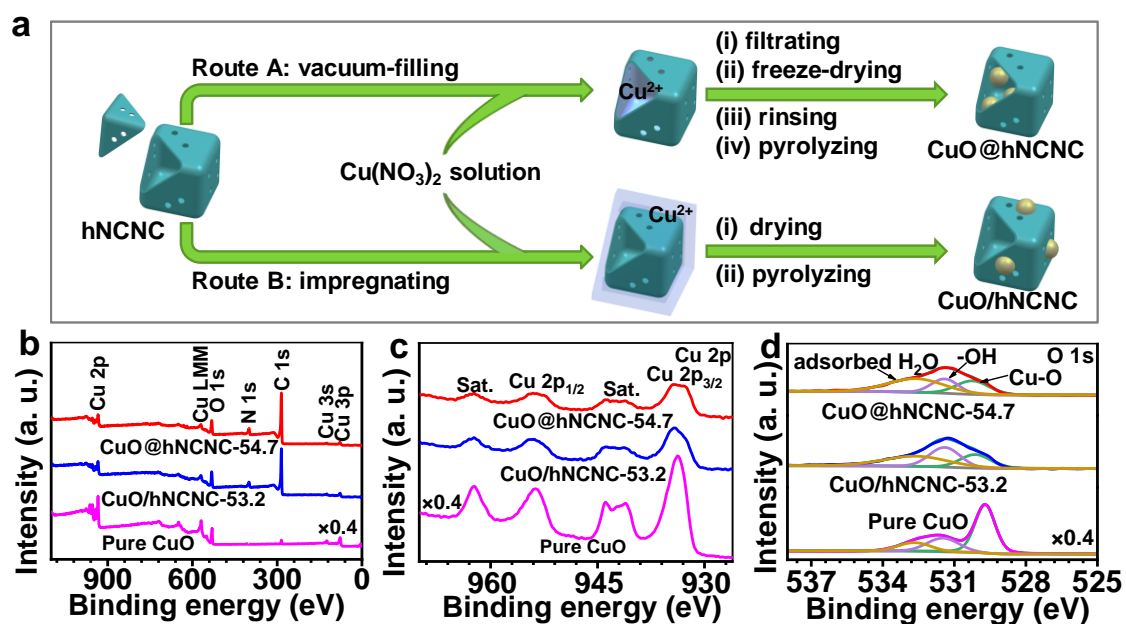
**Fig. S2 XPS characterization of CuO@hNCNC-54.7 and CuO/hNCNC-53.2.** (a) Schematic illustration for preparing CuO@hNCNC (Route A) and CuO/hNCNC (Route B). (b-d) Survey, Cu 2p and O 1s spectra, respectively.

Cu $2p_{3/2}$ (~934.2 eV) and Cu $2p_{1/2}$ (~954.1 eV) correspond to the Cu (II) states (Fig. S2b,c).[1] The O 1s spectra present three distinct peaks at 529.7, 531.4, and 532.6 eV corresponding to the Cu-O bond, OH groups, and adsorbed $H_2O$, respectively (Fig. S2d).[1] For the pure CuO, the O 1s intensity of the Cu-O bond is much stronger than that of the OH groups and adsorbed $H_2O$. For the CuO@hNCNC-54.7 and CuO/hNCNC-53.2, the O 1s intensity of the Cu-O bond is comparable to that of the OH groups and adsorbed $H_2O$. This discrepancy results from the much higher CuO content and the large grain size, as well as the much less adsorbed $H_2O$ due to the absent high surface area hNCNC for the former.
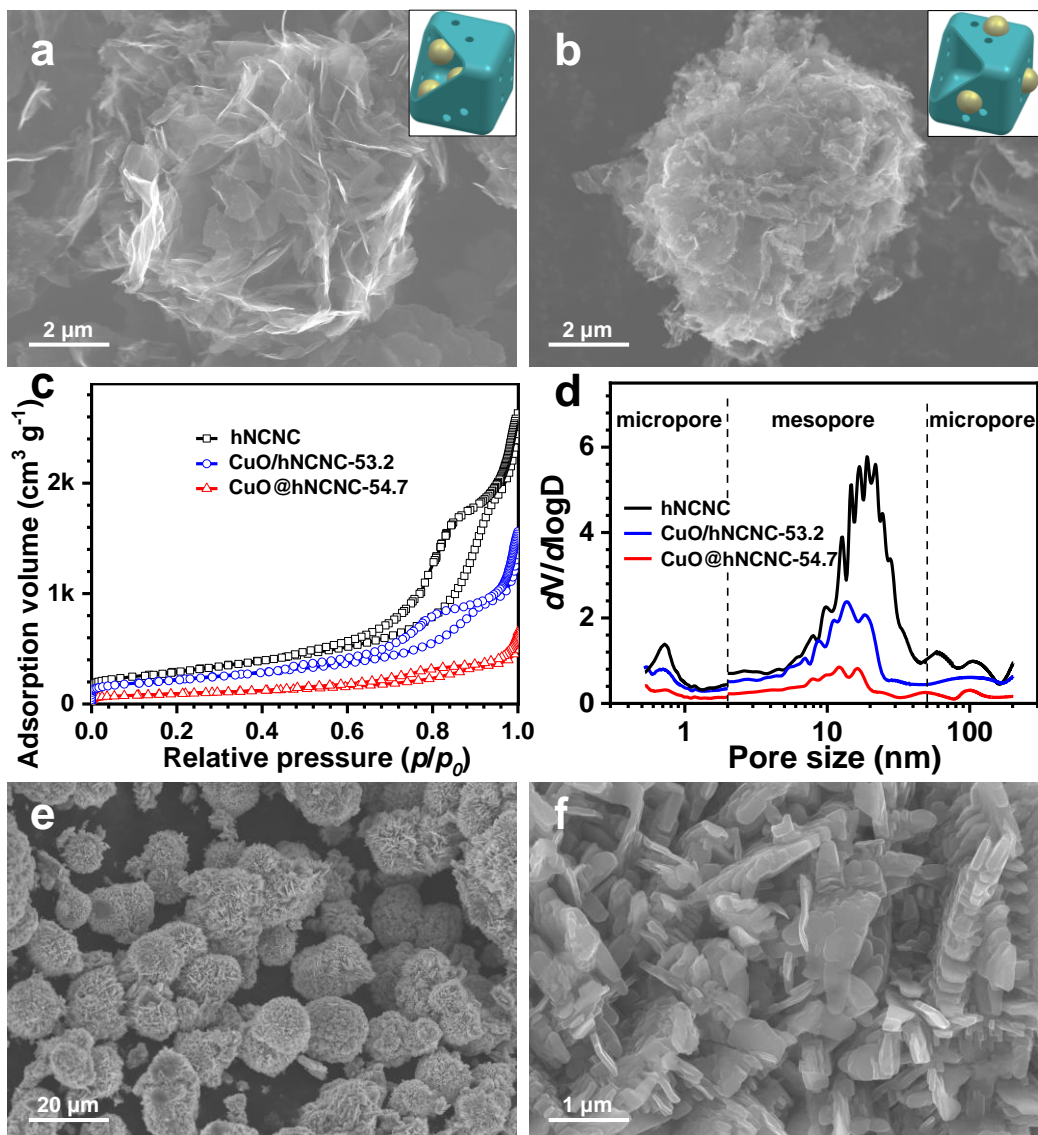
**Fig. S3 Morphology and structure characterizations.** (a,b) SEM images of CuO@hNCNC-54.7 (a) and CuO/hNCNC-53.2 (b). Insets illustrate the corresponding structural units. (c,d) $N_2$ adsorption-desorption isotherms and corresponding pore size distributions. The data of hNCNC are presented for comparison. (e,f) SEM images of the control sample of micron-sized pure CuO particles.

CuO nanoparticles cannot be observed on the surface of hNCNC for CuO@hNCNC-54.7 (Fig. S3a). In contrast, CuO nanoparticles can be observed on the surface of hNCNC for CuO/hNCNC-53.2 (Fig. S3b). The mesoporous distribution of CuO@hNCNC-54.7 shifts to the small-sized side in comparison with those of CuO/hNCNC-53.2 and hNCNC as expected, due to the partial occupation of the inside cavities of hNCNC by CuO nanoparticles (Fig. S3c, d).

The control sample of pure CuO consists of micron-sized sheet-like particles (Fig. S3e, f).
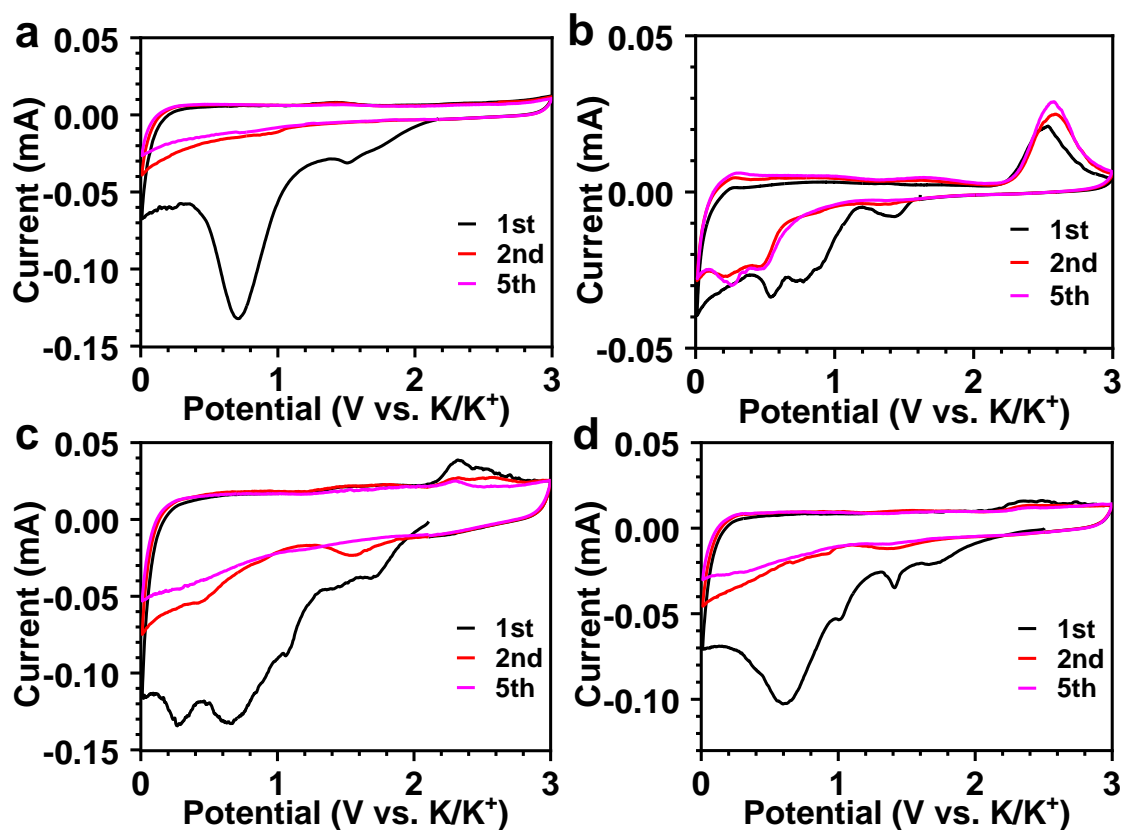
**Fig. S4 Enlarged CV characterizations of samples at a scan rate of 0.05 mV s$^{-1}$.** (a) hNCNC. (b) Pure CuO. (c) CuO@hNCNC-54.7. (d) CuO/hNCNC-53.2. (b-d) is the enlarged Fig. 2a.

In the 1$^{st}$ CV cycle, the discharge curve of hNCNC presents two broad reduction peaks centered at 1.51 and 0.71 V, corresponding to the reaction of K$^+$ with surface functional groups and the SEI formation, respectively (Fig. S4a).[2-5] The discharge curve of the micron-sized pure CuO particles presents four reduction peaks corresponding to the K$^+$ insertion into CuO at 1.44 V and the subsequent formations of KCuO at 0.81 V (CuO + K$^+$ + $e^-$ → KCuO), SEI at 0.54 V and Cu at 0.1 V (KCuO + K$^+$ + $e^-$ → Cu + K$_2$O) (Fig. S4b). Influenced by the hNCNC, the four reduction peaks shift to higher potentials at 1.71, 1.06, 0.66 and 0.27 V for CuO@hNCNC-54.7, and 1.73, 1.01, 0.59 and 0.2 V for CuO/hNCNC-53.2, respectively (Fig. S4c, d).
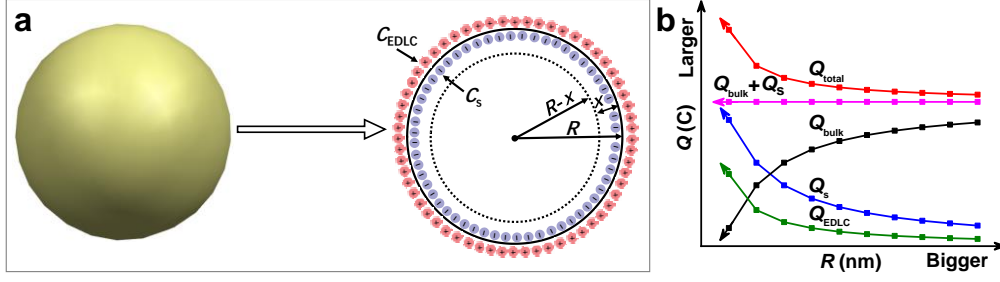
**Fig. S5 Theoretical analysis of capacity contributions from different parts of a spherical CuO particle.** (a) A schematic spherical CuO particle with radius $R$. (b) Plots of the charge quantities from different parts ($Q$) versus radius ($R$).

$R$, $x$, $C_{EDLC}$, and $C_s$ represents the radius, the thickness of shallow surface ($R \geqslant x$), the electric double layer capacitance of surface, and the shallow surface capacitance, respectively (Fig. S5a).

The surface area of the sphere is $S_0 = 4\pi R^2$, and the mass is $m_0 = \frac{4}{3}\pi R^3 \rho$.

So, the $C_{EDLC}$ can be calculated by the following Equations:

$$S_{total} = N_i \times S_0 = \frac{m_{total}}{m_0} \times 4\pi R^2 = \frac{m_{total}}{\frac{4}{3}\pi R^3 \rho} \times 4\pi R^2 = \frac{3m_{total}}{R\rho} \tag{1}$$

$$C_{EDLC} = \varepsilon_r \varepsilon_0 \frac{S_{total}}{d} = \varepsilon_r \varepsilon_0 \frac{3m_{total}}{R\rho d} \tag{2}$$

Here, $\rho$, $S_{total}$, $N_i$, and $m_{total}$ represent the density, toal suface areas, numbers and total mass of all CuO particles, respetively. $\varepsilon_r$, $\varepsilon_0$, and $d$ represent relative permittivity of electrolyte, vacuum permittivity, and distance between the electrical double layers, in turn. In addition:

$$m_s = [\frac{4}{3}\pi R^3 - \frac{4}{3}\pi(R\text{-}x)^3]\rho \tag{3}$$

$$m'_{total} = N_i \times m_s = \frac{m_{total}}{m_0} \times m_s = \frac{m_{total}}{\frac{4}{3}\pi R^3 \rho}[\frac{4}{3}\pi R^3 - \frac{4}{3}\pi(R\text{-}x)^3]\rho = m_{total}[1-(1-\frac{x}{R})^3] \tag{4}$$

Hence, $C_s = \dfrac{Q}{\Delta U} = \dfrac{znEF}{\Delta U} = \dfrac{zm'_{total}EF}{M\Delta U} = \dfrac{zm_{total}F}{M}[1-(1-\frac{x}{R})^3]$ (5)

Here, $m_s$ ($m'_{total}$) is the mass of shallow surface of a single particle (all CuO particles). $z$, $M$, $F$, and $E$ ($\Delta U$) represent the charge number of electrode reaction, the relative molecular mass of CuO, Faraday constant (96485 C mol$^{-1}$), and difference of potential, respectively.

During the reaction, the total charge quantity ($Q_{total}$) is the sum of three parts：

$$Q_{total} = Q_{bulk} + Q_s + Q_{EDLC} \tag{6}$$

Here, $Q_{bulk}$, $Q_s$, and $Q_{EDLC}$ represent the charge quantities from bulk phase reaction, $C_s$, and $C_{EDLC}$, respectively.

Both $Q_{bulk}$ and $Q_s$ come from Faraday redox reaction. For the fixed $m_{total}$,

$$Q_{bulk} + Q_s = \text{Constant} \tag{7}$$

According to equations (2), (5), (6) and (7), with decreasing $R$, $Q_{EDLC}$ ($=C_{EDLC} \times \Delta U$), $Q_s$ ($=C_s \times \Delta U$), and $Q_{total}$ increase, while $Q_{bulk}$ decreases, as schemed in Fig. S5b.

Actually, the increased surface-controlled charge storages have been often observed for various nanosized active components despite the lack of detailed explanation.[6-8]
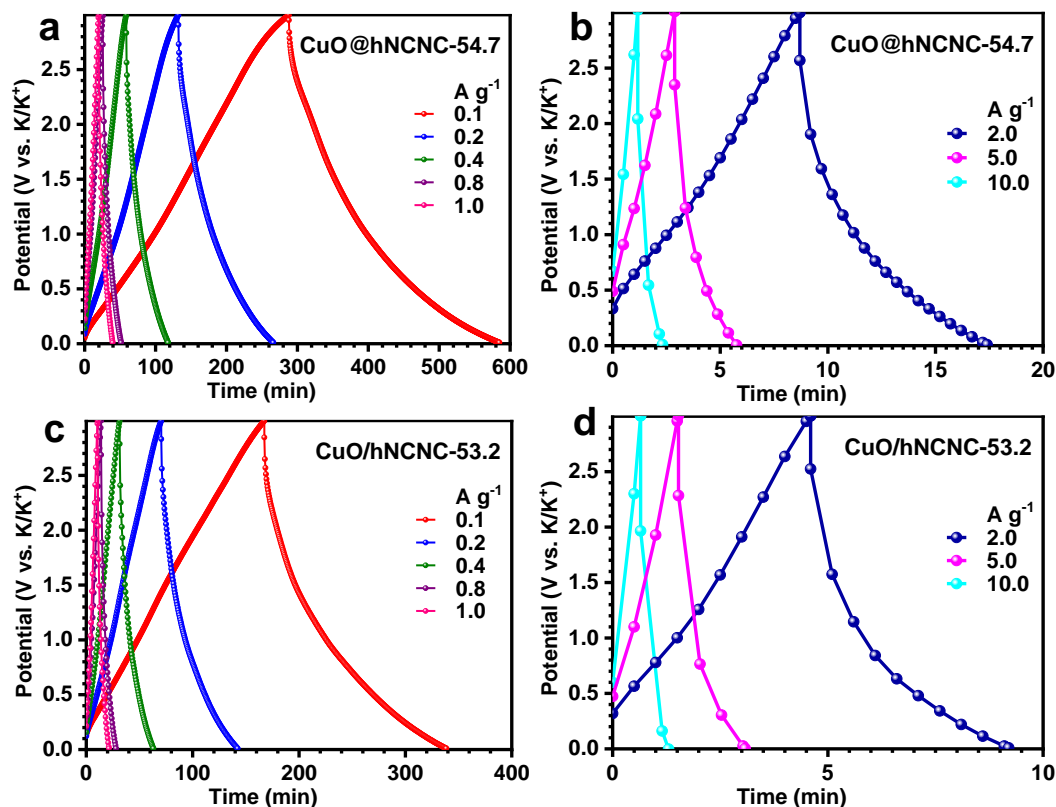
**Fig. S6 GCD curves of half cells at different current densities.** (a,b) CuO@hNCNC-54.7. (c,d) CuO/hNCNC-53.2.
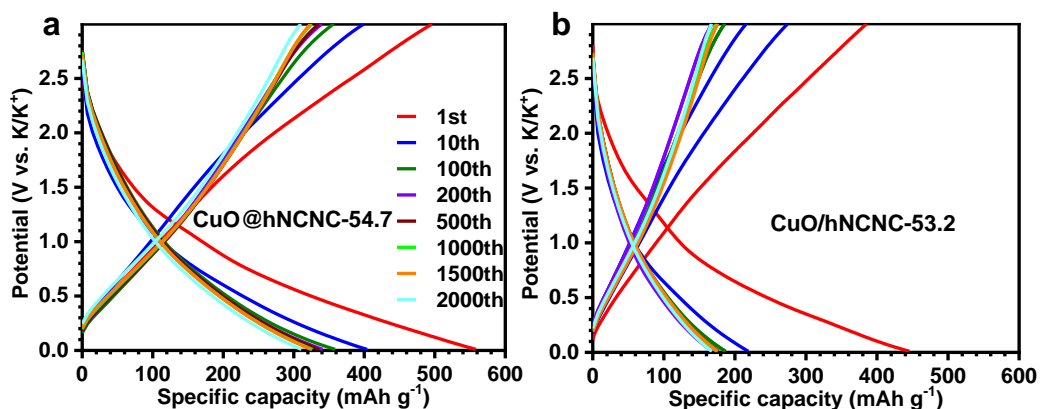
The GCD curves at different current densities are replotted in the potential-time relationship, which clearly indicates the absence of voltage platforms for the curve of 10 A g$^{-1}$. With the same time intervals for data recording, the current density of 10 A g$^{-1}$ gives the fewer data points, leading to the visual voltage platform (**Fig. 2c**).



**Fig. S7 GCD curves at 1.0 A g$^{-1}$.** (a) CuO@hNCNC-54.7. (b) CuO/hNCNC-53.2. Note: The specific capacity is calculated based on the total mass of CuO and hNCNC.
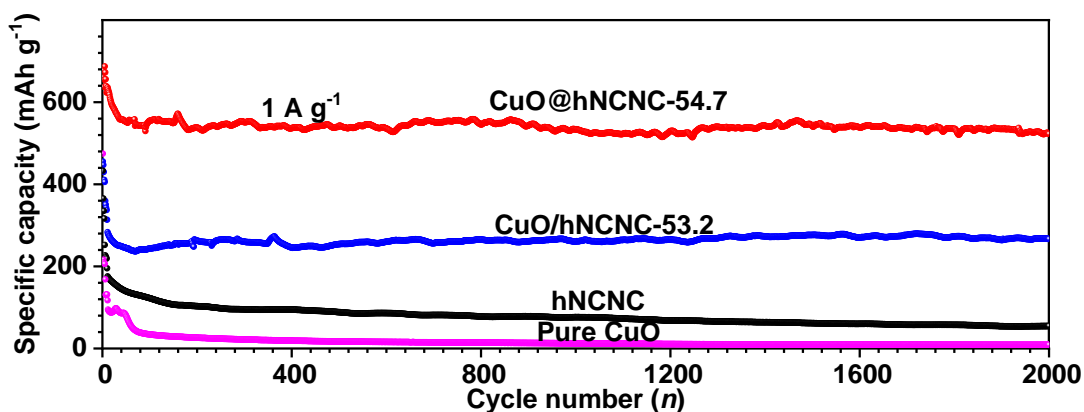
**Fig. S8 Cycling performance of CuO@hNCNC and CuO/hNCNC after 2000 cycles at 1.0 A g$^{-1}$.** The specific capacity is calculated based on the mass of CuO. Note: The data come from Fig. 3d.

Fig. S8 is the replotting of Fig. 2d by deducting the contribution of hNCNC from the total capacity. The so-obtained capacity is based on the mass of CuO active components. It is seen that CuO@hNCNC-54.7 deliver an ultrahigh capacity of 522 mAh g$^{-1}$ after 2000 cycles at 1.0 A g$^{-1}$, much larger than the corresponding 266 mAh g$^{-1}$ for CuO/hNCNC-53.2.
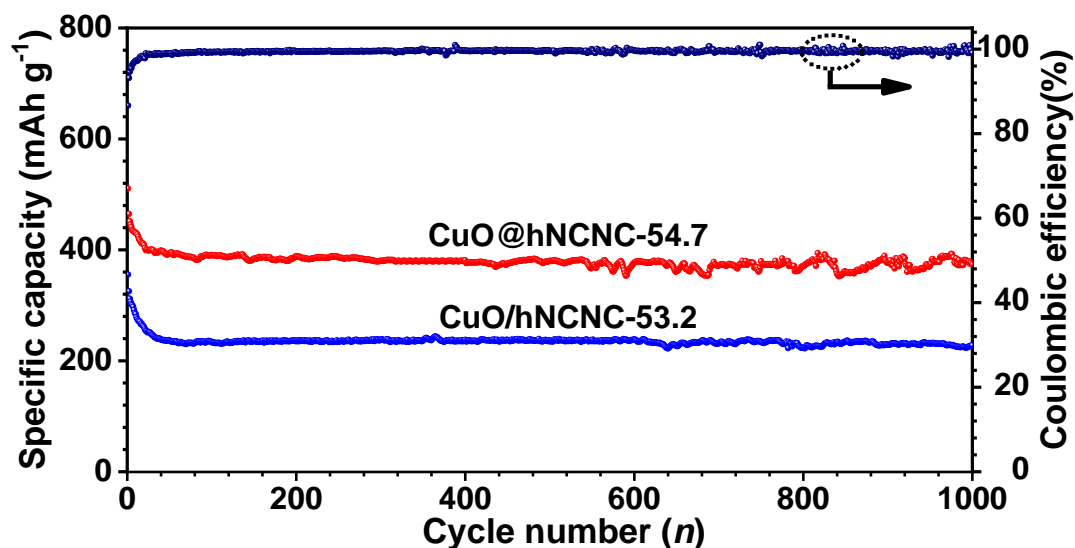


**Fig. S9 Cycling stability of CuO@hNCNC-54.7 and CuO/hNCNC-53.2 at 0.2 A g$^{-1}$.** Note: The specific capacity is calculated based on the total mass of CuO and hNCNC.
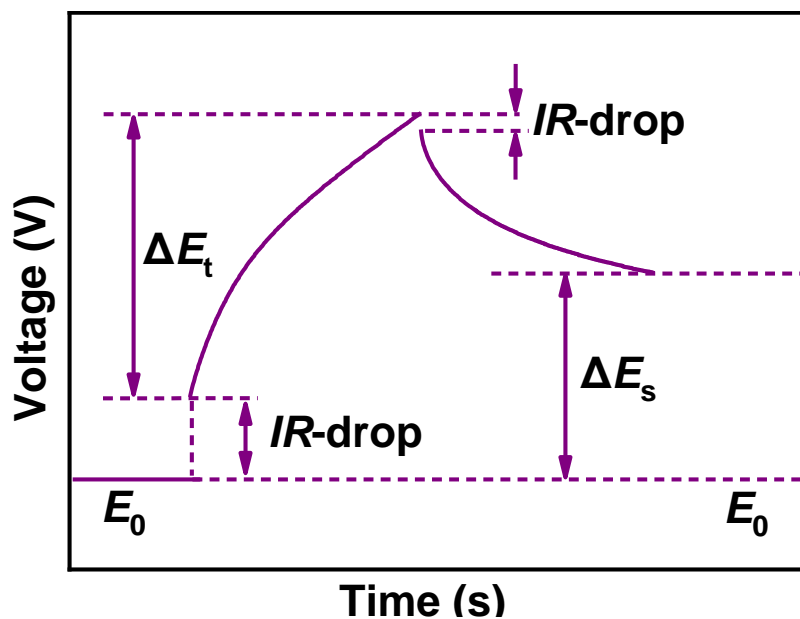
**Fig. S10 The determination of $\Delta E_t$, $\Delta E_s$ and $IR$ drop from the measured GITT profile.**

$D_{K^+}$ is estimated by the formula.[9]

$$D_{K^+} = \frac{4}{\pi\tau}\left(\frac{m_B V_m}{M_B S}\right)^2\left(\frac{\Delta E_s}{\Delta E_t}\right)^2$$

Here, $\tau$ is the current pulse duration, $m_B$, $M_B$, and $V_m$ represent the mass, molar mass, and molar volume of the electrode material, $S$ is the geometric area of the disc electrode, and $\Delta E_t$ and $\Delta E_s$ are the voltage change of the GITT curve in a single step except for $IR$ drop under constant current pulse and steady state, respectively.
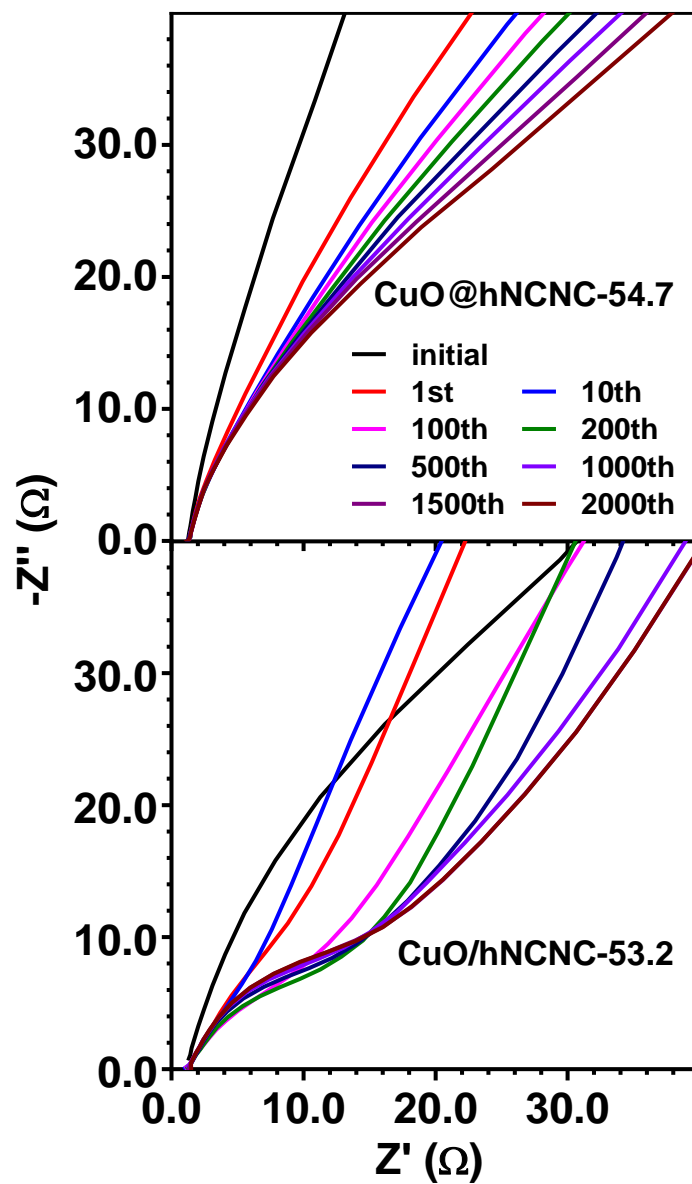
**Fig. S11 Local-enlarged EIS spectra of CuO@hNCNC-54.7 and CuO/hNCNC-53.2 during the long-term cycle at 1.0 A g$^{-1}$**. The data come from Fig. 4a.
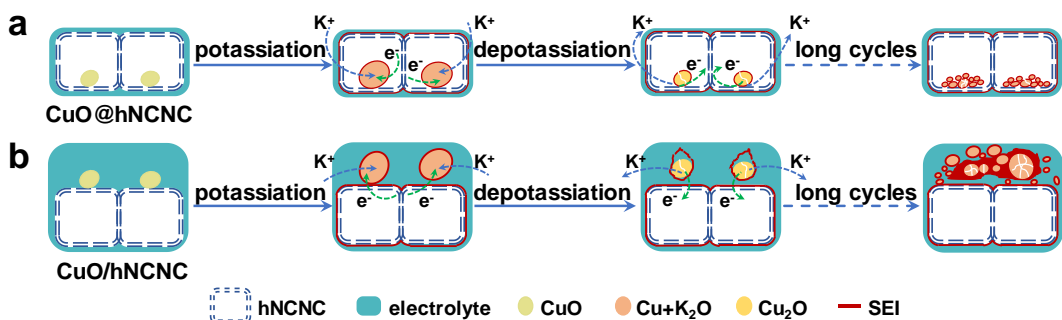
**Fig. S12** Schematics of the loss-free pulverization for CuO@hNCNC (a) and the commonly harmful pulverization for CuO/hNCNC (b), respectively.

Over long-term cycling, the yolk-shelled CuO@hNCNC undergoes a loss-free pulverization due to the much smaller sizes of the micropores of hNCNC wall than those of the pulverized Cu-based active components, hence forms the relatively stable SEI film (Fig. S12a). Specifically, at the initial stage of potassiation/deintercalation, the SEI film forms on the inside CuO and also on the hNCNC surface. With the cycling going on, $K^+$ can permeate through the SEI film and reacts with the inside CuO due to the desolvation effect of $KPF_6$,[10] but the solvents are hard to penetrate the SEI film on the hNCNC surface, resulting in a relatively stable SEI film on the CuO surface. In contrast, the supported CuO/hNCNC cannot inhibit the loss and agglomeration of the pulverized Cu-based active components due to the open structure, hence forms the unstable SEI film due to the continuous exposure of new interfaces to the electrolyte (Fig. S12b).
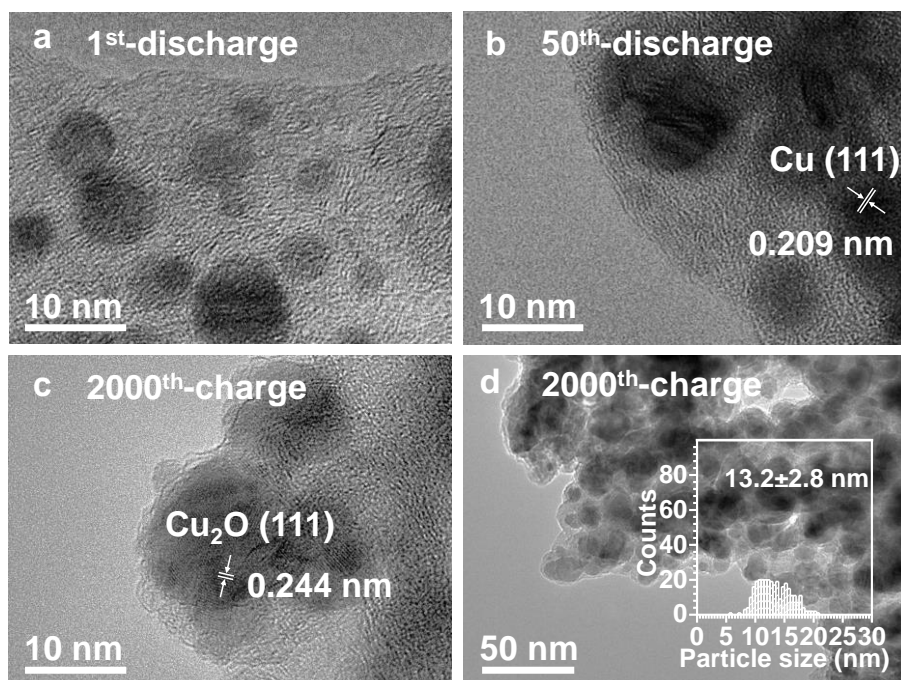


**Fig. S13 HRTEM images of CuO/hNCNC-53.2.** (a) After the 1st. (b) After the 50th discharge. (c,d) After the 2000th charge. Inset in (d) is the particle size histogram.
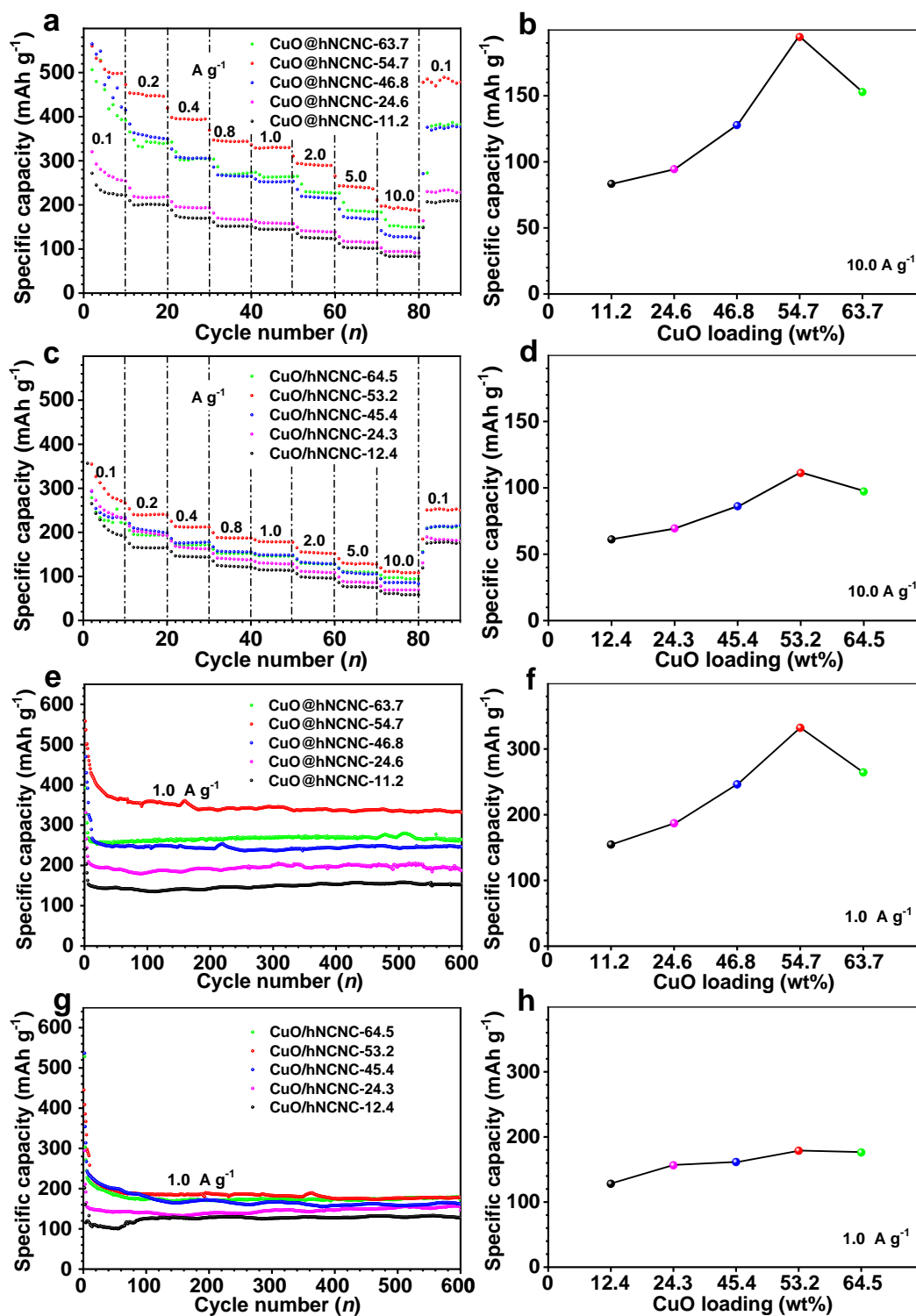
**Fig. S14 Rate capability and cycling performance for CuO@hNCNC and CuO/hNCNC samples.** (a-d) Rate capability and corresponding loading-dependent specific capacity at 10.0 A g$^{-1}$ for CuO@hNCNC (a,b) and for CuO/hNCNC (c,d). (e-h) Cycling performance and corresponding loading-dependent specific capacity at 1.0 A g$^{-1}$ for CuO@hNCNC (e,f) and for CuO/hNCNC (g,h).

Note: The specific capacity is calculated based on the total mass of CuO and hNCNC.
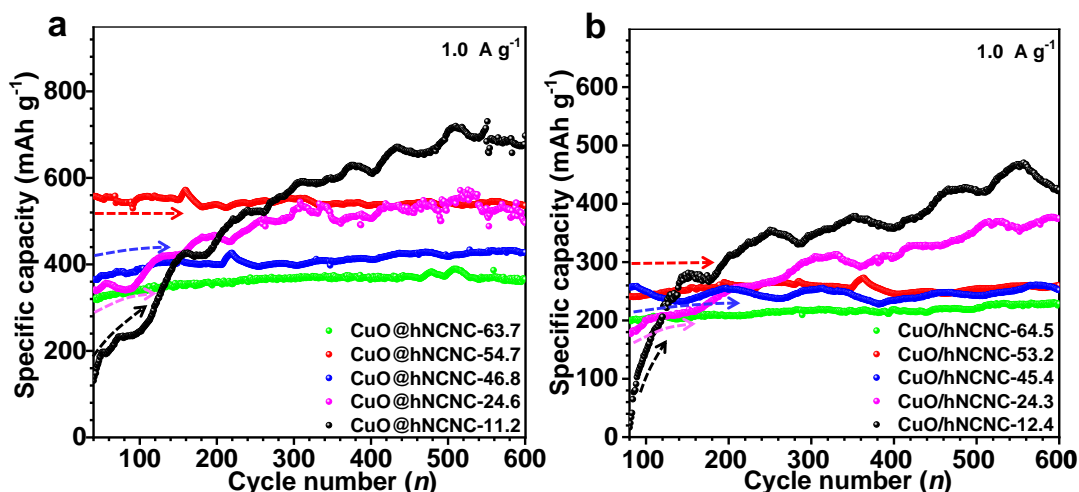
**Fig. S15 Cycling performance for 600 cycles at 1.0 A g⁻¹.** (a) CuO@hNCNC. (b) CuO/hNCNC. Note: The specific capacity is based on the mass of CuO.

Fig. S15 is the replotting of Fig. S14e,g by deducting the contribution of hNCNC from the total capacity,[11] which denotes the capacity based on CuO.

**For CuO@hNCNC samples:** In the initial stage (before ~100 cycles), the lower CuO loading leads to the smaller capacity in the range of 11.2-54.7 wt% (Fig. S15a), which could be associated with the smaller the particle size of CuO (i.e., the higher the specific surface area) to consume a relatively larger amount of electrolyte for the SEI film formation.[2, 12] For the higher loading of 63.7 wt% (CuO@hNCNC-63.7), the interior space of hNCNC is not enough to accommodate the volume-expanded discharge products, leading to the rebound of the capacity.

Along with the cycling, the lower CuO loading will lead to the smaller ultimate size of the pulverized CuO nanoparticles, thus the more contribution of the surface-controlled charge storage (Fig. S5, Fig. S16). Hence, with increasing CuO loading in 11.2-54.7 wt%, the increasing tendency of capacity changes from very obvious (steep) to inconspicuous (flat), as schematically arrowed (Fig. S15a).

Specifically, with the low CuO loading of 11.2 and 24.6 wt%, CuO@hNCNC-11.2 and CuO@hNCNC-24.6 obviously rebound their capacities to the high level after 600 cycles, with the higher capacity for the former. With increasing the CuO loading to 46.8 and 54.7 wt%, the initial sizes of CuO particles and the ultimate sizes after pulverization will increase accordingly. Hence, the capacity increase from the surface-controlled charge storage become weaker and weaker. As a result, CuO@hNCNC-46.8 and CuO@hNCNC-54.7 only presents a slight and negligible increase of capacity, respectively. The situation for CuO@hNCNC-63.7 with the highest CuO loading of 63.7 wt% is somewhat different due to insufficient interior space of hNCNC to accommodate the volume-expanded discharge products, leading to the low capacity.

**For CuO/hNCNC samples:** The evolution of cycling performance with CuO loading for the CuO/hNCNC samples is similar to the case for the CuO@hNCNC samples, but generally with the lower capacity for the former (Fig. S15). This result is mainly attributed to the open conductive network structure for the former which cannot inhibit the repeated pulverization, loss and agglomeration of the Cu-based particles, as well as the exposure of new interfaces to the electrolyte.[13, 14]
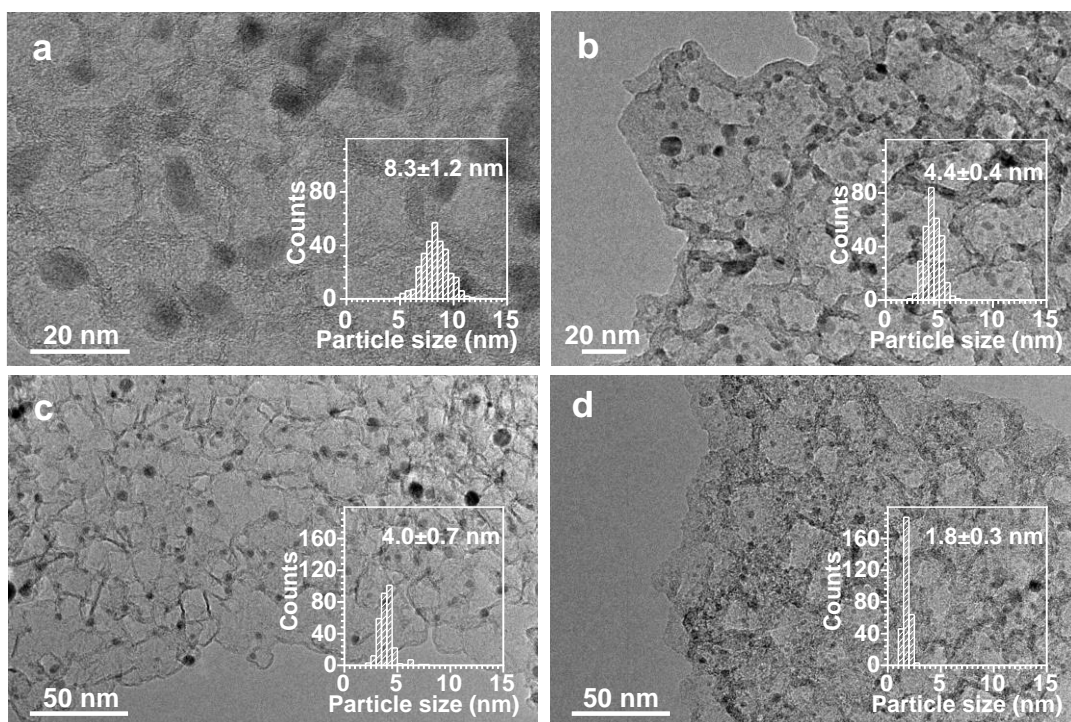
**Fig. S16 TEM characterization of CuO@hNCNC before and after cycling.** (a,b) TEM images of CuO@hNCNC-54.7 before (a) and after 2000 cycles (b). (c,d) TEM images of CuO@hNCNC-11.2 before (c) and after 600 cycles (d).

Note: Insets in (a-d) correspond to the particle size histograms. The TEM image in (a) and (b) comes from Fig. 1c and Fig. 4f, respectively.

The particle size of CuO varies depending on the amount of loading. The lower CuO loading and the smaller particle size (Fig. S16a, c). Over prolonged cycling, the Cu-based active components undergo loss-free pulverization, resulting in the smaller particle size (Fig. S16b, d).
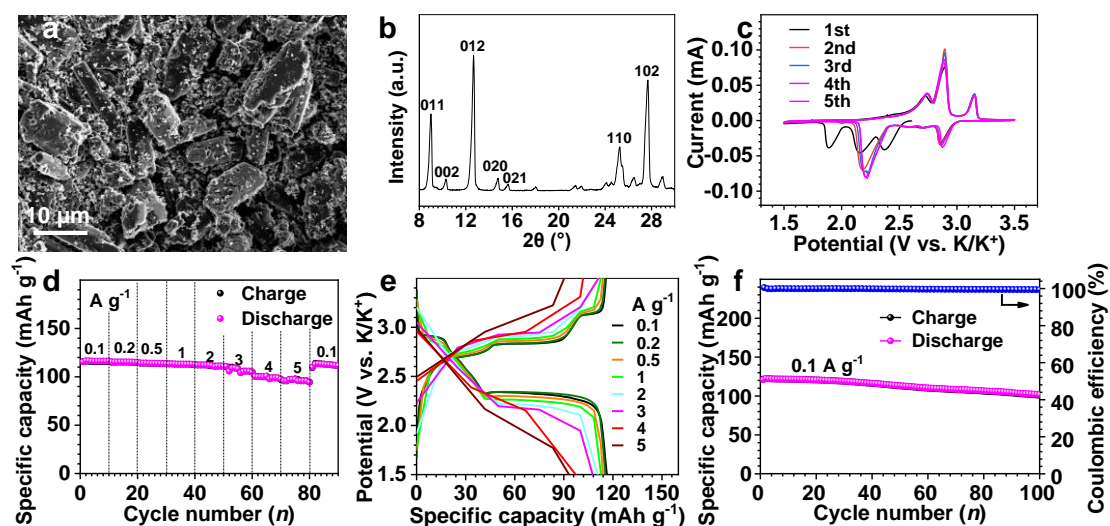
**Fig. S17 Morphology, structure and electrochemical performance of PTCDA.** (a) SEM image. (b) XRD pattern. (c) CV curves at a scan rate of 0.1 mV s⁻¹. (d, e) Rate capability and GCD curves. (f) Cycling performance at 0.1 A g⁻¹.

The organic cathode was prepared by annealing PTCDA at 450 °C for 4 h under Ar with a heating rate of 5 °C min⁻¹.[15] The C=O bonds in the PTCDA could transform to C-O-K during the potassiation, and it will return to C=O during the depotassiation (Fig. S17c).[15]

The PTCDA exhibits the excellent specific capacities of 116, 115, 114, 113, 112, 108, 101, 97 mA h g⁻¹ and back to 113 mAh g⁻¹ at the current densities of 0.1, 0.2, 0.5, 1.0, 2.0, 3.0, 4.0, 5.0 A g⁻¹ and back to 0.1 A g⁻¹, respectively (Fig. S17d, e). It also shows the excellent cycling stability with the specific capacity of 102 mAh g⁻¹ after 100 cycles at 0.1 A g⁻¹ (Fig. S17f). At high current density, the insertion and extraction of potassium ions become more difficult, and the surface pseudocapacitance or adsorption dominates the reaction process, leading to the disappearance of the voltage plateau at 2.9 V, similar to in the literature cases for PTCDA.[15]
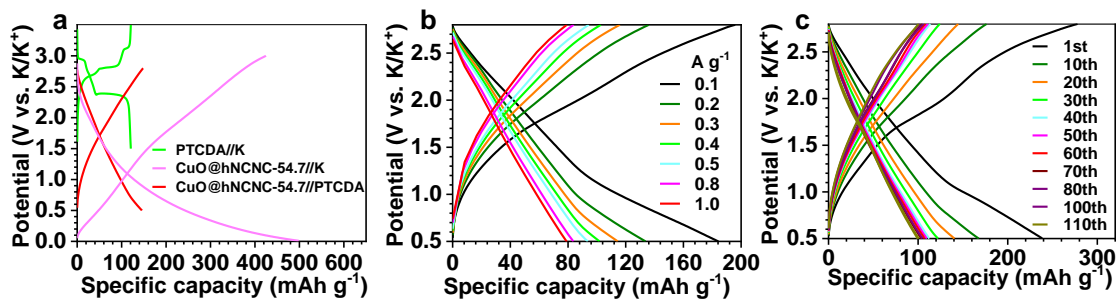
**Fig. S18 Electrochemical performances for CuO@hNCNC-54.7//PTCDA full cell.** (a) GCD curve. The GCD curves of PTCDA//K and CuO@hNCNC-54.7//K are presented for reference. (b) GCD curves of the 5th cycle at different current densities. (c) GCD curves at the designated cycle at 0.1 A $g^{-1}$. Note: The specific capacity is calculated based on the total mass of CuO@hNCNC.

The voltage range of PTCDA//K half cell (cathode) and CuO@hNCNC-54.7//K half cell (anode) is 1.5-3.5 V and 0.01-3.0 V, respectively. Accordingly, the voltage range of CuO@hNCNC-54.7//PTCDA full cell is set to 0.5-2.8 V to avoid decomposition of the electrolyte (Fig. S18a).

**Table S1.** Parameters of CuO@hNCNC and CuO/hNCNC

| Samples | $S_{BET}$ (m$^2$ g$^{-1}$) | $\kappa$ (S m$^{-1}$) | Cu content (at.% from XPS data) |
|---|---|---|---|
| CuO@hNCNC | 328 | 75 | 2.42 |
| CuO/hNCNC | 788 | 28 | 3.48 |
| pure CuO | / | 0.092 | / |
| hNCNC | 1074 | 212 | / |

Note: The electrical conductivity ($\kappa$) was measured by a four-wire method using a source measure unit (Keithley 6430).[16]

**Table S2.** Comparison of the electrochemical performances of CuO@hNCNC with the reported conversion-type anode materials for PIBs.

| Sample | Content (wt.%) | $S_{BET}$ (m$^2$ g$^{-1}$) | Particle size (nm) | Rate capability (mAh g$^{-1}$@A g$^{-1}$) | | | Cycle stability (mAh g$^{-1}$@A g$^{-1}$/cycles) | Ref. |
|---|---|---|---|---|---|---|---|---|
| **CuO@hNCNC** | **54.7** | **328** | **8.3 ± 1.2** | **498@0.1** **450@0.2** **395@0.4** | **345@0.8** **330@1.0** **290@2.0** | **240@5.0** **191@10.0** | **373@0.2/1000** **310@1.0/2000** (based on CuO+hNCNC) **522@1.0/2000** (based on CuO) | **This study** |
| CuO nanoplates | / | / | / | 351.9@0.2 284.6@0.4 | 227.1@0.8 206.8@1.0 | 163@2.0 | 342.5@0.2/60 206@1.0/100 | 1 |
| CuO@CF | / | 43 | / | 358@0.05 287@0.3 | 253@0.5 182@1.0 | 110@2.0 90@4.0 | 207@1.0/300 | 17 |
| CuO/Cu-NCNFs | 16.1 | / | ~400 | 87.5@2.0 | | | 206@0.1/100 | 18 |
| CuS@GO | / | / | 20-40/ | 407.7@0.1 322.75@0.2 | 291.4@0.3 256.2@0.5 | 196.5@1.0 | 400@0.1/50 | 19 |
| C-WS$_2$@CNFs | 72.2 | / | 90-200 | 319@0.05 304@0.1 249@0.5 | 234@1.0 219@2.0 204@4.0 | 175@8.0 168@10.0 | 247@0.1/300 168@2.0/300 | 20 |
| FeSe$_2$@C-$_3$ MCs | 71.5 | 9.22 | 900-1300 | 376.8@0.05 | 141.8@2.0 | | 228@0.1/100 | 21 |
| Bi$_2$MoO$_6$ | / | / | 500-3000 | 319.8@0.05 242.1@0.1 | 214.4@0.2 165.3@0.5 | | 121.7@0.1/600 | 22 |
| MoTe$_2$ | / | / | 24060-148140 | 244.2@0.05 222.9@0.1 | 186.8@0.2 131.4@0.5 | 106.3@1.0 87.3@2.0 | 104@0.1/50 | 23 |
| Co$_3$O$_4$-Fe$_2$O$_3$ composite | 66.7 | / | 10-40 | / | | | 220@0.05/50 | 24 |
| Co$_3$O$_4$@N-C | / | / | 500-2000 | 408.2@0.089 | | | 213@0.5/740 | 25 |
| NMCSA@Co/Co$_3$O$_4$ | 23 | / | | 585@0.05 404@0.1 | 347@0.2 274@0.5 | 250@1.0 222@2.0 | 164@0.5/1500 141@1.0/1800 | 26 |
| α-Fe$_2$O$_3$ HBs@NC | 83 | | 2000 | / | | | 214@0.05/500 | 27 |

| Material | | | | | | | | Ref |
|---|---|---|---|---|---|---|---|---|
| CoS@G | 75 | 105.79 | 10-20 | / | | | 310.8@0.5/100 | 28 |
| CoSe@NCNTs | 67.27 | 194.3 | 30-70 | 348@0.5<br>329@1.0 | 306@1.5<br>292@2.0 | 278@3.0 | 282@2.0/500 | 29 |
| NCNF@CoSe$_2$ | / | 83.5 | 150-200 | 297@0.2<br>286@0.4 | 279@0.6<br>259@0.8 | 238@1.0<br>196@2.0 | 253@0.2/60<br>173@2.0/600 | 30 |
| FeS$_2$@C | / | / | 2000 | 182@10.0 | | | 295@1.0/150 | 31 |
| FeP@CNBs | / | / | 500-700 | 201@0.1<br>156@0.2 | 101@0.5<br>65@1.0 | 37@2.0 | 205@0.1/300 | 32 |
| FeCl$_3$@C | 32.53 | 85.23 | / | 269.5@0.05 | 133.1@5.0 | | 224 @0.1/500 | 33 |
| MoSe$_2$/N-C | 91.8 | / | / | 300@0.1<br>244@0.2 | 211@0.5<br>195@1.0 | 178@2.0 | 258@0.1/300 | 34 |
| N-Co$_3$Se$_4$/GO | 72.9 | 71.8 | 23 | 442.8@0.1<br>414.2@0.2<br>352.4@0.5 | 294.2@1.0<br>256.7@2.0<br>230.2@3.0 | 203.3@5.0 | 301.8@1.0/500 | 35 |
| NiS$_2$/3DGO | 90.14 | / | 100-120 | 494@0.05<br>398@0.1 | 339@0.2<br>283@0.5 | 235@1.0 | 260@1.0/160 | 36 |
| MoS$_2$-WS$_2$-C | 95 | 54.6 | 200-1000 | 377@0.1 | 176@5.0 | | 291@1.0/50 | 37 |
| FMSC | / | 51 | 400-500 | 313 @0.1<br>309@0.2 | 282@0.5<br>227@1.0 | | 178@1.0/400 | 38 |
| MoS$_2$/N-doped-C | 75 | 51.9 | / | 258@0.1<br>238@0.2 | 204@0.5<br>171@1.0 | 131@2.0 | 330@0.05/50 | 39 |
| SbVO$_4$@RGO | 81 | / | / | 407@0.1<br>339@0.2 | 192@0.5<br>118 @1.0 | | 340.2@0.1/100 | 40 |
| MoSe$_2$-rGO | / | / | / | 427 @0.1 | 258@2.0 | | 212@1.0/150 | 41 |
| Bi$_2$O$_2$Se/graphite | 90 | / | / | 530@0.1<br>484@0.2<br>440@0.5 | 380@1.0<br>314@2.0<br>214@5.0 | 89@10.0 | 300@0.1/100 | 42 |
| Sb$_2$S$_3$-rGO | 80 | / | 25 | 509@0.1 | 459@0.5 | 286@1.0 | 100@0.05/40 | 43 |
| CAS-Ti$_3$C$_2$ | 75 | 46.16 | / | 571.8@0.05 | 241.8@1.0 | 163.3@5.0 | 175.6@1.0/1800 | 44 |

| Material | | | | | | | | Ref. |
|---|---|---|---|---|---|---|---|---|
| | | | | 378.7@0.5 | 188.0@2.0 | | | |
| $MnO_2$@rGO | / | / | / | 242@0.02 <br> 136@0.05 | 93@0.1 <br> 65@0.2 | 44@0.5 <br> 34@1.0 | 60@0.2/400 | 45 |
| ZnTe/$CoTe_2$@NC | 58 | 131.7 | 238.9 | 498.7@0.1 <br> 430.8@0.2 | 352.1@0.5 <br> 279.9@1.0 | 233.3@2.0 <br> 190.2@5.0 | 261.3 @1.0/1000 <br> 165.2@5.0/5000 | 46 |
| $V_5S_8$@C | 73 | / | 250-350 | 550@0.05 <br> 474@0.1 <br> 422@0.2 | 360@0.5 <br> 312@1.0 <br> 274@2.0 | 205@5.0 <br> 153@10.0 | 360@0.5/500 <br> 190@2.0/1000 | 47 |
| $VSe_{1.6}$/C@N-C⊏$MoSe_2$ | 41.4 | 16.9 | / | 381.7@0.1 <br> 328.4@0.2 | 274.7@0.5 <br> 233.6@1.0 | 200.0@2.0 <br> 161.4@5.0 | 180@1.0/5000 | 48 |
| SnSe/$MoSe_2$@GN | 67.1 | 94.11 | 6.6-12.9 | 501.2 @0.1 | 163.3@1.6 | | 248@1.0/200 | 49 |
| $SnO_2$@C | 76.2 | / | 500-700 | 250@0.05 <br> 196@0.1 | 181@0.2 <br> 145@0.3 | 118@0.5 <br> 88@1.0 | 156@0.5/700 <br> 152@1.0/1600 | 50 |
| $MoS_2$-C/rGO | 76 | 35.17 | 40 | 353.81@0.1 <br> 313.69@0.25 | 291.52@0.5 <br> 268.57@1.0 | 248.34@2.0 | 161.67 @2.0/2000 | 51 |
| Sn/$MoS_2$@C | 52.4 | 261.1 | 100 | / | | | 226@1.0/300 | 52 |
| $Cu_3PS_4$/G | / | / | 50-1000 | 563@0.5 <br> 468@0.1 <br> 416@0.25 | 365@0.5 <br> 301@1.0 <br> 231@2.0 | 167@4.0 <br> 90@8.0 | 180@0.5/3000 <br> 617.8@0.05/100 | 53 |
| VN@CFs | 42.9 | 45.1 | / | 245.8@0.05 <br> 227.5@0.1 <br> 188.4@0.2 | 170.8@0.5 <br> 153.5@1.0 <br> 134.5@2.0 | 115.7@4.0 <br> 102.7@6.0 | 232@0.05/800 <br> 133.2@2.0/1600 | 54 |
| $SnS_2$@C | 41.77 | / | 280-330 | 457.4@0.05 <br> 376.5@0.1 <br> 354.2@0.2 | 319.1@0.5 <br> 289.7@1.0 <br> 264.3@2.0 | 219.4@5.0 | 343@0.1/200 <br> 183@2.0/2000 | 55 |
| $BiSbO_4$ nanonetwork | / | / | / | 331.5@0.05 <br> 307.8@0.1 | 275.9@0.3 <br> 240.2@0.5 | 167.1@1.0 | 369@0.05/100 <br> 257@0.5/1000 | 56 |

| | | | | | | | | | |
|---|---|---|---|---|---|---|---|---|---|
| | | | | 292.5@0.2 | 203.1@0.75 | | | | |
| FeNCN | / | / | / | 472@0.1<br>428@0.2<br>396@0.3 | 369@0.4<br>339@0.5<br>268@1.0 | 194@2.0<br>99@5.0 | 409@0.1/350<br>266@0.5/500 | | 57 |
| VSe$_2$ | / | 413.3 | / | 374@0.1<br>350@0.2 | 334@0.5<br>269@1.0 | | 335@0.2/200 | | 58 |
| ZnTe@C/Ti$_3$C$_2$T$_x$ | 87.9 | / | / | 300.5@0.1<br>286.6@0.2 | 261.1@0.3<br>226.5@0.5 | 179.2@1.0 | 301.7@0.5/160<br>230.2@1.0/3500 | | 59 |
| CoS$_2$-CNs | 55.9 | 241.1 | 200 | 508.4@0.1<br>415.2@0.2 | 314.4@0.5<br>276.5@1.0 | 227.5@2.0<br>188.5@3.0 | 280.5@1.0/800 | | 60 |
| Bi$_2$S$_3$/Bi$_2$Se$_3$ | / | / | / | 604@0.05<br>477@0.1<br>372@0.25 | 302@0.5<br>255@1.0<br>221@1.5 | 196@2.0<br>175@2.5<br>89@3.5 | 201.7@0.5/1000 | | 61 |
| Sb$_2$S$_3$@MXene | / | 31.0 | / | 434.1@0.05<br>372.6@0.1 | 326.4@0.2<br>294.6@0.5 | 207.9@1.0<br>119.0@2.0 | 422.1@0.1/100 | | 62 |
| MoP-MoS$_2$@SNC | 38.1 | 190 | 50-80 | 339.8@0.1<br>273.2@0.2 | 239.2@0.5<br>204.7@1.0 | 168.9@2.0 | 286.2@0.1/100<br>150@1.0/500 | | 63 |
| Cu$_9$S$_5$/MoS$_2$/C heterostructure | / | / | 10-40 | 325.1@0.1<br>300.2@0.2<br>273.5@0.5 | 245.6@1.0<br>211.2@2.0<br>142.3@5.0 | 100.2@10.0 | 327.3@0.1/50<br>270.6@0.5/200<br>155@1.0/1000 | | 64 |
| Sn$_{0.95}$Cu$_{0.05}$Se@CNF | / | 23.1 | 11 | 292.3@0.1<br>269.6@0.2<br>262.7@0.3 | 245.4@0.5<br>222.6@1.0<br>193.6@2.0 | 173.7@3.0<br>143.2@5.0 | 267@0.1/100<br>224@0.5/500 | | 65 |
| BiOCl/Ti$_3$C$_2$T$_x$ | / | / | 150-300 | / | | | 225@0.1/1335 | | 66 |
| CoTe$_2$@NPCNFs@NC | 66.3 | 190.5 | 10 | 526.0@0.05<br>438.9@0.1 | 353.4@0.2<br>266.9@0.5 | 209.3@1.0<br>148.9@2.0 | 409.1@0.05/50<br>198@0.5/600 | 120@2.0/1000 | 67 |

| | | | | | | | | |
|---|---|---|---|---|---|---|---|---|
| VS-WS$_2$-Se NS | / | / | / | 363.9@0.05 316.8@0.1 | 283.8@0.2 245.3@0.5 | 207.1@1.0 154.2@2.0 | 328.6@0.1/50 144.2@2.0/100 | 68 |
| CoSe-C@C | 65.6 | 216.3 | 200-500 | 388@0.2 348@0.5 | 334@1.0 316@2.0 | 280@5.0 233@10.0 | 432@0.2/1000 | 69 |
| FeSe/C | 74.3 | 253 | 20-100 | 391@0.1 377@0.2 | 345@0.5 325@1.0 | 307@5.0 230@10.0 | 550@0.2/100 | 70 |
| V$_5$Se$_8$@C | / | 176.3 | / | 328@0.1 316@0.2 | 293@0.5 257@1.0 | 201@2.0 162@4.0 | 387@0.2/300 145@4.0/800 | 71 |
| Sb$_2$S$_3$-Bi$_2$S$_3$ @C@rGO | 75.9 | 83.76 | / | 599.1@1.0 556.4@2.0 | 536.8@3.0 514.5@5.0 | 485.8@8.0 | 461@8.0/1100 | 72 |
| NCS@NC | 84.1 | 37.74 | 500 | 594.3@0.1 583.5@0.2 | 546.9@0.4 506.2@0.8 | 495.8@1.0 440.8@2.0 | 637.5 @0.1/100 417.7 @2.0/1000 | 73 |
| NCOP | / | / | 100 | 721.5@0.1 629.8@0.2 541.5@0.5 | 456.4@1.0 395.2@2.0 339.5@5.0 | 265.7@10.0 | 332.5@1.0/500 | 74 |

Note: NCNFs: nitrogen-doped carbon microfibers; GO: graphene oxide; CNFs: carbon nanofibers; FeSe$_2$@C-3 MCs: carbon-coated iron selenide microcapsules; Co$_3$O$_4$@N-C: Co$_3$O$_4$@N-doped carbon; NMCSA@Co/Co$_3$O$_4$: Co/Co$_3$O$_4$ NPs enclosed in 3D ordered N-doped mesoporous carbon sphere array; HBs@NC: N-doped C-coated hollow bowls; MoS$_2$ confined in reduced graphene oxide; CoS@G: cobalt sulfide @ graphene; NCNTs: N-doped carbon nanotubes; NCNF: N-doped carbon nanotubes framework; CNBs: carbon nanoboxes; 3DGO: three dimensional graphene oxide; FMSC: Fe-Mo selenide@N-doped carbon core/shell nanostructure; CAS-Ti$_3$C$_2$: Cu$_{12}$Sb$_4$S$_{13}$ quantum dots/few-layered Ti$_3$C$_2$ nanosheets; CuO@CF: CuO@copper foam. VSe$_{1.6}$/C@N-C$_3$MoSe$_2$: nanotubes with encapsulated VSe$_{1.6}$/C cores and protecting shells of N-C and MoSe$_2$ nanosheets; MoSe$_2$@GN: MoSe$_2$ nanosheets grown on graphene; MoS$_2$-C/rGO: MoS$_2$ nanoparticles anchored onto graphene sheet; VN@CFs: VN particle composed nanosheets on carbon fibers; FeNCN: iron carbodiimide; CoS$_2$-CNs: CoS$_2$ nanoparticles inside individual carbon shells; MoP-MoS$_2$@SNC: MoP-MoS$_2$@Aspergillus niger spore-derived N-doped carbon (SNC) composite; Sn$_{0.95}$Cu$_{0.05}$Se@CNF: Cu-doped SnSe nanoparticles encapsulated in carbon

nanofibers; CoTe$_2$@NPCNFs@NC: a dual-type N-doped carbon-confined CoTe$_2$ composite material (CoTe$_2$@NPCNFs@NC, where NPCNFs stands for N-doped porous carbon nanofibers and NC represents N-doped porous carbon); VS-WS$_2$-Se NS: Se-filled WS$_2$ nanosheets with sulfur vacancies; NCS@NC: Ni$_3$S$_4$/Co$_9$S$_8$ confined in nitrogen-doped carbon nanocubes; NCOP: Ni-Co oxide/Ni-Co oxy-phosphide.

In references 69-71, three selenides manifest excellent potassium storage performances which are conversion-alloy type anode materials with high theoretical specific capacity when forming K$_x$Se$_y$ alloy. In references 72-74, three conversion-type anode materials also have very high theoretical specific capacity. Thus, their potassium storage performances are better than those of Cu-based conversion-type anode materials.

**Table S3.** Comparison of $R_s$, $R_{ct}$, amd $R_f$ of CuO@hNCNC-54.7 and CuO/hNCNC-53.2.

| Cycle No. | $R_s$ | | $R_{ct}$ | | $R_f$ | |
|---|---|---|---|---|---|---|
| | CuO@hNCNC-54.7 | CuO/hNCNC-53.2 | CuO@hNCNC-54.7 | CuO/hNCNC-53.2 | CuO@hNCNC-54.7 | CuO/hNCNC-53.2 |
| $0^{th}$ | 1.2 | 1.3 | 2737.0 | 4425.0 | 10.5 | 24.1 |
| $1^{st}$ | 1.2 | 1.4 | 461.0 | 1379.0 | 1.5 | 2.9 |
| $10^{th}$ | 1.2 | 1.3 | 472.0 | 891.0 | 1.3 | 4.2 |
| $100^{th}$ | 1.2 | 1.5 | 472.8 | 774.0 | 1.9 | 5.3 |
| $200^{th}$ | 1.3 | 1.6 | 422.1 | 1091.0 | 2.0 | 8.3 |
| $500^{th}$ | 1.3 | 1.7 | 422.7 | 1447.0 | 2.2 | 10.6 |
| $1000^{th}$ | 1.3 | 1.5 | 493.3 | 1292.0 | 2.4 | 10.4 |
| $1500^{th}$ | 1.3 | 1.6 | 457.3 | 1594.0 | 2.5 | 12.1 |
| $2000^{th}$ | 1.2 | 1.7 | 479.0 | 1699.0 | 2.7 | 12.1 |

Table S4. Comparison of electrochemical performances for the full cell

| Full cell (anode//cathode) | Rate capability (mAh g$^{-1}$@A g$^{-1}$) | | | Cycle stability (mAh g$^{-1}$@A g$^{-1}$/cycles) | Coulombic efficiency (%) | Ref. |
|---|---|---|---|---|---|---|
| **CuO@hNCNC-54.7//PTCDA** | **160@0.1 134@0.2 114@0.3** | **102@0.4 94@0.5 84@0.8** | **80@1.0** | **100@0.1/110** | **99** | **This study** |
| C-WS$_2$@CNFs//ACNF | 65@0.2 | 38@6.0 | | / | / | 20 |
| Bi$_2$MoO$_6$//PTCDA | / | | | 131.1@0.05/20 | 98 | 22 |
| NMCSA@Co/Co$_3$O$_4$-2//AC | / | | | / | 99 | 26 |
| CoSe@NCNTs//PB | 272@0.2 220@0.5 | 183@0.8 161@1.0 | | 228@0.5/200 | 98 | 29 |
| V$_5$S$_8$@C// PTCDA | 380@0.1 310@0.2 | 210@0.4 155@0.6 | 130@1.0 | 200@0.2/90 | 95 | 47 |
| VSe$_{1.6}$/C@N-C⊂ MoSe$_2$// PTCDA | / | | | 158@0.2/50 | 99 | 48 |
| SnSe/MoSe$_2$@GN// K$_4$[Fe(CN)$_6$]·3H$_2$O | / | | | 64.21@0.05/100 | 92 | 49 |
| Cu$_3$PS$_4$/G // PB | 58@0.03 39@0.075 37@0.12 | 30@0.15 27@0.3 25@0.45 | 20 @0.75 | 57@0.12/800 | 99 | 53 |
| SnS$_2$@C//KPB | / | | | 323.9@0.1/30 | 90 | 55 |
| BiSbO$_4$//PBNPs | 58@0.03 39@0.075 37@0.12 | 30@0.15 27@0.3 25@0.45 | 20 @0.75 | 50@0.2/200 | 99 | 56 |
| FeNCN//PB | 48@0.1 41@0.2 | 34@0.3 30@0.4 | 25@0.5 | | 92 | 57 |
| ZnTe@C/Ti$_3$C$_2$T$_x$//KPB | 87.0@0.02 | 69.6@0.05 | 47.6@0.1 | 70.3@0.1/150 | / | 59 |

| | | | | | | |
|---|---|---|---|---|---|---|
| | 80.0@0.03 | 55.5@0.08 | 29.3@0.2 | | | |
| Bi$_2$S$_3$/Bi$_2$Se$_3$ vdWHs //KFeHCF | 91@0.05 80@0.125 | 64@0.25 56@0.5 | 52@1.0 43@1.25 | 64@0.25/850 | 89 | 61 |
| Cu$_9$S$_5$/MoS$_2$/C//PTCDA | / | | | 135@0.1/80 | 99 | 64 |
| V$_5$Se$_8$@C//K$_{0.5}$MnO$_2$ | 99@0.02 87@0.05 | 80@0.1 72@0.2 | 60@0.4 | 60@0.4/200 | 99 | 71 |

In reference 29, the CoSe@NCNTs-based full cell delivers excellent potassium storage performances which is PB cathode material with high theoretical specific capacity (170 mAh g$^{-1}$ for PB, 135 mAh g$^{-1}$ for PTCDA). In reference 47, the V$_5$S$_8$@C-based full cell also shows the excellent potassium storage performances which is V$_5$S$_8$ anode material with high theoretical specific capacity, however, its coulombic efficiency (CE) is only 95%, which is lower than that of the CuO@hNCNC-54.7-based full cell (CE=99%).

## References

1    K. Cao, H. Liu, W. Li, Q. Han, Z. Zhang, K. Huang, Q. Jing and L. Jiao, *Small*, 2019, **15**, e1901775.

2    F. Xu, Y. Zhai and E. Zhang, *Angew Chem Int Ed*, 2020, **59**, 19460-19467.

3    Y. Wang, Z. Wang, Y. Chen, H. Zhang, M. Yousaf, H. Wu, M. Zou, A. Cao and R. P. S. Han, *Adv Mater*, 2018, **30**, e1802074.

4    X. Han, T. Chen, P. Zhang, Y. Qi, P. Yang, Y. Zhao, M. Shao, J. Wu, J. Weng, S. Li and F. Huo, *Adv Funct Mater*, 2021, **32**, 2109672.

5    Y. Liu, C. Yang, Q. Pan, Y. Li, G. Wang, X. Ou, F. Zheng, X. Xiong, M. Liu and Q. Zhang, *J Mater Chem A*, 2018, **6**, 15162-15169.

6    J. Zhang, J. Zhang, H. Wang, V. W.-h. Lau, G.-H. Lee, K. Zhang, M. Park and Y.-M. Kang, *ACS Energy Lett*, 2022, **7**, 4472-4482.

7    F. Hartmann, M. Etter, G. Cibin, L. Liers, H. Terraschke and W. Bensch, *Adv Mater*, 2021, **33**, e2101576.

8    W. Ren, Z. Zhu, M. Qin, S. Chen, X. Yao, Q. Li, X. Xu, Q. Wei, L. Mai and C. Zhao, *Adv Funct Mater*, 2019, **29**, 1806405.

9    X. Hu, Y. Liu, J. Chen, L. Yi, H. Zhan and Z. Wen, *Adv Energy Mater*, 2019, **9**, 1901533.

10   H. Wang, D. Yu, X. Wang, Z. Niu, M. Chen, L. Cheng, W. Zhou and L. Guo, *Angew Chem Int Ed*, 2019, **58**, 16451-16455.

11   S. Dong, D. Yu, J. Yang, L. Jiang, J. Wang, L. Cheng, Y. Zhou, H. Yue, H. Wang and L. Guo, *Adv Mater*, 2020, **32**, e1908027.

12   W. Yang, J. Zhou, S. Wang, W. Zhang, Z. Wang, F. Lv, K. Wang, Q. Sun and S. Guo, *Energy Environ Sci*, 2019, **12**, 1605-1612.

13   Y. Liu, Z. Tai, Q. Zhang, H. Wang, W. K. Pang, H. K. Liu, K. Konstantinov and Z. Guo, *Nano Energy*, 2017, **35**, 36-43.

14   L. Guo, L. Cao, J. Huang, J. Li, K. Kajiyoshi, J. He and H. Qi, *ACS Appl Energy Mater*, 2021, **4**, 10391-10403.

15   L. Fan, R. Ma, J. Wang, H. Yang and B. Lu, *Adv Mater*, 2018, **30**, e1805486.

16   Z. Lyu, D. Xu, L. Yang, R. Che, R. Feng, J. Zhao, Y. Li, Q. Wu, X. Wang and Z. Hu, *Nano Energy*, 2015, **12**, 657-665.

17   Z. Gu, G. Li, N. Hussain, B. Tian and Y. Shi, *Appl Surf Sci*, 2022, **592**, 153323.

18   L. Gao, Z. Wang, H. Hu, H. Cheng, L. Zhang and X. Yang, *J Electroanal Chem*, 2020, **876**, 11483.

19   X. Jia, E. Zhang, X. Yu and B. Lu, *Energy Technol*, 2019, **8**, 1900987.

20   S. Geng, T. Zhou, M. Jia, X. Shen, P. Gao, S. Tian, P. Zhou, B. Liu, J. Zhou, S. Zhuo and F. Li, *Energy Environ Sci*, 2021, **14**, 3184-3193.

21   S. Lu, H. Wu, S. Xu, Y. Wang, J. Zhao, Y. Li, A. M. Abdelkader, J. Li, W. A. Wang, K. Xi, Y. Guo, S. Ding, G. Gao and R. V. Kumar, *Small*, 2021, **17**, 2005745.

22   J. X. Hu, Y. Y. Xie, J. Q. Zheng, Y. Q. Lai and Z. A. Zhang, *Nano Res*, 2020, **13**, 2650-2657.

23   B. Wu, J. Luxa, E. Kovalska, M. Ivo, H. Zhou, R. Malek, P. Marvan, S. Wei, L.

Liao and Z. Sofer, *Energy Storage Mater*, 2021, **43**, 284-292.

24　I. Sultana, M. M. Rahman, S. Mateti, V. G. Ahmadabadi, A. M. Glushenkov and Y. Chen, *Nanoscale*, 2017, **9**, 3646-3654.

25　D. Adekoya, H. Chen, H. Y. Hoh, T. Gould, M. J. T. Balogun, C. Lai, H. Zhao and S. Zhang, *ACS Nano*, 2020, **14**, 5027-5035.

26　H. Liu, W. Zhang, Y. Song, L. Li, C. Zhang and G. Wang, *Adv Funct Mater*, 2021, **31**, 202107728.

27　M. Qin, Z. Zhang, Y. Zhao, L. Liu, B. Jia, K. Han, H. Wu, Y. Liu, L. Wang, X. Min, K. Xi, C. Y. Lao, W. Wang, X. Qu and R. V. Kumar, *Adv Funct Mater*, 2019, **29**, 1902822.

28　H. Gao, T. Zhou, Y. Zheng, Q. Zhang, Y. Liu, J. Chen, H. Liu and Z. Guo, *Adv Funct Mater*, 2017, **27**, 1902822.

29　Y. Liu, Q. Deng, Y. Li, Y. Li, W. Zhong, J. Hu, X. Ji, C. Yang, Z. Lin and K. Huang, *ACS Nano*, 2021, **15**, 1121-1132.

30　Q. Yu, B. Jiang, J. Hu, C. Y. Lao, Y. Gao, P. Li, Z. Liu, G. Suo, D. He, W. A. Wang and G. Yin, *Adv Sci*, 2018, **5**, 1800782.

31　Z. Zhao, Z. Hu, R. Jiao, Z. Tang, P. Dong, Y. Li, S. Li and H. Li, *Energy Storage Mater*, 2019, **22**, 228-234.

32　F. Yang, H. Gao, J. Hao, S. Zhang, P. Li, Y. Liu, J. Chen and Z. Guo, *Adv Funct Mater*, 2019, **29**, 1808291.

33　D. Li, M. Zhu, L. Chen, L. Chen, W. Zhai, Q. Ai, G. Hou, Q. Sun, Y. Liu, Z. Liang, S. Guo, J. Lou, P. Si, J. Feng, L. Zhang and L. Ci, *Adv Mater Interfaces*, 2018, **5**, 1800606.

34　J. Ge, L. Fan, J. Wang, Q. Zhang, Z. Liu, E. Zhang, Q. Liu, X. Yu and B. Lu, *Adv Energy Mater*, 2018, **8**, 1801477.

35　H. Zhang, Y. Cheng, Q. Zhang, W. Ye, X. Yu and M. S. Wang, *ACS Nano*, 2021, **15**, 10107-10118.

36　K. Han, J. Meng, X. Hong, X. Wang and L. Mai, *Nanoscale*, 2020, **12**, 8255-8261.

37　J. H. Choi, G. D. Park and Y. C. Kang, *Chem Eng J*, 2021, **408**, 127278.

38　J. Chu, Q. Yu, D. Yang, L. Xing, C.-Y. Lao, M. Wang, K. Han, Z. Liu, L. Zhang, W. Du, K. Xi, Y. Bao and W. Wang, *Appl Mater Today*, 2018, **13**, 344-351.

39　B. Jia, Q. Yu, Y. Zhao, M. Qin, W. Wang, Z. Liu, C.-Y. Lao, Y. Liu, H. Wu, Z. Zhang and X. Qu, *Adv Funct Mater*, 2018, **28**, 1803409.

40　X. Yi, J. Ge, J. Zhou, J. Zhou and B. Lu, *Sci China Chem*, 2020, **64**, 238-244.

41　J. Sheng, T. Wang, J. Tan, W. Lv, L. Qiu, Q. Zhang, G. Zhou and H. M. Cheng, *ACS Nano*, 2020, **14**, 14026-14035.

42　Z. Wu, G. Liang, J. Wu, W. K. Pang, F. Yang, L. Chen, B. Johannessen and Z. Guo, *Adv Energy Mater*, 2021, **11**, 2100185.

43　V. Lakshmi, A. A. Mikhaylov, A. G. Medvedev, C. Zhang, T. Ramireddy, M. M. Rahman, P. Cizek, D. Golberg, Y. Chen, O. Lev, P. V. Prikhodchenko and A. M. Glushenkov, *J Mater Chem A*, 2020, **8**, 11424-11434.

44　Y. Cao, Y. Zhang, H. Chen, S. Qin, L. Zhang, S. Guo and H. Yang, *Adv Funct Mater*, 2021, **32**, 2108574.

45    Z. Wang, X. Yan, F. Wang, T. Xiong, M. S. Balogun, H. Zhou and J. Deng, *Carbon*, 2021, **174**, 556-566.

46    C. Zhang, H. Li, X. Zeng, S. Xi, R. Wang, L. Zhang, G. Liang, K. Davey, Y. Liu, L. Zhang, S. Zhang and Z. Guo, *Adv Energy Mater*, 2022, **12**, 2202577.

47    L. Li, W. Zhang, X. Wang, S. Zhang, Y. Liu, M. Li, G. Zhu, Y. Zheng, Q. Zhang, T. Zhou, W. K. Pang, W. Luo, Z. Guo and J. Yang, *ACS Nano*, 2019, **13**, 7939-7948.

48    W. Kang, X. Han, X. Wang, Z. Zhu, B. Zhang, Z. Wang, Y. Wang and D. Sun, *J Mater Chem A*, 2022, **10**, 18185-18194.

49    X. Hu, R. Zhu, B. Wang, H. Wang and X. Liu, *Chem Eng J*, 2022, **440**, 135819.

50    Y. Huang, S. Ding, S. Xu, Z.-F. Ma, J. Wang and X. Yuan, *Chem Eng J*, 2022, **446**, 137265.

51    J. Li, F. Hu, H. Wei, J. Hei, Y. Yin, G. Liu, N. Wang and H. Wei, *Composites Part B*, 2023, **250**, 110424.

52    X. Wu, H. Wu, B. Xie, R. Wang, J. Wang, D. Wang, Q. Shi, G. Diao and M. Chen, *ACS Nano*, 2021, **15**, 14125-14136.

53    S.-F. Ho and H.-Y. Tuan, *Chem Eng J*, 2023, **452**, 139199.

54    C. Xu, J. Mu, T. Zhou, S. Tian, P. Gao, G. Yin, J. Zhou and F. Li, *Adv Funct Mater*, 2022, **32**, 2206501.

55    D. Li, L. Dai, X. Ren, F. Ji, Q. Sun, Y. Zhang and L. Ci, *Energy Environ Sci*, 2021, **14**, 424-436.

56    C. H. Chang, K. T. Chen, Y. Y. Hsieh, C. B. Chang and H. Y. Tuan, *ACS Nano*, 2022, **16**, 1486-1501.

57    E. Zhang, S. Wu, X. Sun, B. Wang, L. Xu, X. Yi, X. Wang and B. Lu, *Chem Eng J*, 2023, **453**, 139966.

58    C. Yang, J. Feng, F. Lv, J. Zhou, C. Lin, K. Wang, Y. Zhang, Y. Yang, W. Wang, J. Li and S. Guo, *Adv Mater*, 2018, **30**, e1800036.

59    R. Hu, D. Sha, X. Cao, C. Lu, Y. Wei, L. Pan and Z. Sun, *Adv Energy Mater*, 2022, **12**, 2203118.

60    H. Zhang, Y. Cheng, J. Sun, W. Ye, C. Ke, M. Cai, H. Gao, P. Wei, Q. Zhang and M. S. Wang, *Adv Energy Mater*, 2022, **12**, 2201259.

61    Y.-Y. Hsieh and H.-Y. Tuan, *Energy Storage Mater*, 2022, **51**, 789-805.

62    P. Zhang, Q. Zhu, Y. Wei and B. Xu, *Chem Eng J*, 2023, **451**, 138891.

63    D. Sun, C. Tang, H. Cheng, W. Xu, A. Du and H. Zhang, *J Energy Chem*, 2022, **72**, 479-486.

64    B. Zhang, B. Xu, H. Qin, L. Cao and X. Ou, *J Mater Sci&Technol*, 2023, **143**, 107-116.

65    N. Ren, L. Wang, J. Dong, K. Cao, Y. Li, F. Chen, J. Xiao, B. Pan and C. Chen, *Chem Eng J*, 2023, **458**, 141489.

66    X. Cao, Y. You, D. Sha, H. Xia, H. Wang, J. Zhang, R. Hu, Y. Wei, Z. Bao, Y. Xu, L. Pan, C. Lu, W. He, M. Zhou and Z. Sun, *Adv Funct Mater*, 2023, **33**, 2303275.

67    Q. Li, J. Peng, W. Zhang, L. Wang, Z. Liang, G. Wang, J. Wu, W. Fan, H. Li, J. Wang and S. Huang, *Adv Energy Mater*, 2023, **13**, 2300150.

68    Q. Zhu, W. Li, J. Wu, N. Tian, Y. Li, J. Yang and B. Liu, *ACS Appl Mater Interfaces*, 2022, **14**, 51994-52006.

69    X. Gu, L. Zhang, W. Zhang, S. Liu, S. Wen, X. Mao, P. Dai, L. Li, D. Liu, X. Zhao and Z. Guo, *J Mater Chem A*, 2021, **9**, 11397-11404.

70    L. Zhang, X. Gu, X. Mao, S. Wen, P. Dai, L. Li, D. Liu and X. Zhao, *J Power Sources*, 2021, **486**, 229373.

71    C. Yang, F. Lv, K. Dong, F. Lai, K. Zhao, F. Sun, S. Dou, Q. Wang, J. Xu, P. Zhang, T. Arlt, X. Chen, Y. Chen, I. Manke and S. Guo, *Energy Storage Mater*, 2021, **35**, 1-11.

72    K. Li, X. Liu, Y. Qin, Z. Zhao, Y. Xu, Y. Yi, H. Guan, Y. Fu, P. Liu and D. Li, *Chem Eng J*, 2021, **414**, 136829.

73    Q. Cheng, X. Liu, Q. Deng, C. Chen, W. Zhong and C. Yang, *Chem Eng J*, 2022, **446**, 136829.

74    S. Wang, S. Lv, G. Wang, K. Feng, S. Xie, G. Yuan, K. Nie, M. Sha, X. Sun and L. Zhang, *Adv Sci*, 2022, **9**, e2105193.